Available online at www.sciencedirect.com
SCIENCE DIRECT®
Journal of Magnetic Resonance 162 (2003) 284–299
JMR Journal of Magnetic Resonance
www.elsevier.com/locate/jmr

Ultra-broadband NMR probe: numerical and experimental study of transmission line NMR probe

Atsushi Kubo* and Shinji Ichikawa

Institute for Molecular Science, Myodaiji, Okazaki 444-8585, Japan

Received 27 September 2002; revised 15 January 2003

Abstract

We have reinvestigated a transmission line NMR probe first published by Lowe and co-workers in 1970s [Rev. Sci. Instrum. 45 (1974) 631; 48 (1977) 268] numerically and experimentally. The probe is expected to be ultra-broadband, thus might enable new types of solid-state NMR experiments. The NMR probe consists of a coil and capacitors which are connected to the coil at regular intervals. The circuit is the same as a cascaded LC low-pass filter, except there are nonzero mutual inductances between different coil sections. We evaluated the mutual inductances by Neumann's formula and calculated the electrical characteristics of the probe as a function of a carrier frequency. We found that they were almost the same as those of a cascaded LC low-pass filter, when the inductance L of a section was estimated from the inductance of the whole coil divided by the number of the sections, and if C was set to the capacitance in a section. For example, the characteristic impedance of a transmission line coil is given by $Z = (L/C)^{1/2}$. We also calculated the magnitude and the distribution of RF magnetic field inside the probe. The magnitude of RF field decreases when the carrier frequency is increased because the phase delay between neighboring sections is proportional to the carrier frequency. For cylindrical coils, the RF field is proportional to $(\pi\nu/2\nu_d)^{1/2}\exp(-\nu/\nu_d)$, where the decay frequency ν_d is determined by the dimensions of the coil. The observed carrier frequency thus must be much smaller than the decay frequency. This condition restricts the size of transmission line coils. We made a cylindrical coil for a ^{1}H NMR probe operating below 400 MHz. It had a diameter 2.3 mm and a pitch 1.2 mm. Five capacitors of 6 pF were connected at every three turns. The RF field strength was 40 and 60 kHz at the input RF power 100 W by a calculation and by experiments, respectively. The calculations showed that the RF field inhomogeneity along the coil axis was caused by a standing wave of current, which arose from the reflections at the coil ends. The calculation showed that the homogeneity could be improved by decreasing the pitch near the both ends and making their impedance close to that at the center.

Keywords: NMR probe; Broadband; Transmission line; RF field homogeneity

1. Introduction

Resonant circuits are used in most nuclear magnetic resonance (NMR) probes, which can be tuned in a frequency bandwidth of a few hundred kilohertz. Solid samples containing heavy nuclei and quadrupolar nuclei have NMR spectral widths sometimes much larger than the bandwidth of resonance probes. In such samples, most of the experiments have been performed by a simple Hahn's echo sequence, by changing a spectrometer frequency and readjusting a probe tuning or by changing a static magnetic field. Although the correlation between different spectral regions might be important in conducting and magnetic solids, two-dimensional experiments [1] are not common in those samples. Since the carrier frequency or the static field must be changed to excite different spectral regions, the experiments require a rapid jump of a probe resonance frequency or a static magnetic field.

There is another probe circuit, which employs a transmission line structure; the RF pulses enter from an input port, travel through the probe, and go out from an output port. This circuit was first employed for a

* Corresponding author. Present address: Department of Chemistry, Graduate School of Science, Kyoto University, Kyoto 606-8502, Japan.
E-mail address: a.kubo@kuchem.kyoto-u.ac.jp (A. Kubo).

1090-7807/03/$ - see front matter © 2003 Elsevier Science (USA). All rights reserved.
doi:10.1016/S1090-7807(03)00014-4

broadband microwave amplifier [2] and then was applied to an ESR probe for double resonance experiments [3,4]. In 1974, Lowe and Engelsberg [5] first published this type of NMR probe and named it "delay line NMR probe." The delay line is a device to introduce a phase lag to RF signals or a time delay to pulse signals by changing the length of a transmission line or by modifying the velocity of a travelling electromagnetic wave. However, in this paper, we will use another name "transmission line NMR probe" which Stokes et al. [6] quoted in their publication.

The circuit of transmission line probe resembles to a low-pass filter (LPF) circuit, of which individual section consists of an inductor and two capacitors (π-type LPF) or two inductors and a capacitor (T-type LPF). It differs from LPF only in the respect that it employs a single coil, so that there are the mutual inductances between different sections. The transmisson line probe was first analyzed by a simple LPF model [5] and later by an improved model [7] which took mutual inductance between neighboring sections. According to these analyses, the probe circuit can be described by the characteristic impedance and the cut-off frequency. It does not have any tuning circuit. If the characteristic impedance is adjusted to 50 Ω when the probe is constructed, it should have a wide bandwidth below the cut-off frequency and a short transient decay time.

They also analyzed the RF field distribution inside the probe. Lowe and Engelsberg investigated cylindrical coils and found experimentally that the RF field was very inhomogeneous. Lowe and Whitson theoretically analyzed the RF field distribution in flat coils and concluded that the field should be relatively homogeneous as long as the coil thickness is much smaller than the wavelength of the electromagnetic wave travelling down the coil axis. Although the intensive mathematical analyses were presented by Lowe and Whitson, numerical evaluations of the RF field distribution were not performed.

After these publications, only one paper by Stokes et al. employed the transmission line probe, probably because of the difficulty of its construction. Recently, Conradi mentioned a possible use of this probe at low temperature, since the characteristic impedance of the coil might not be altered by the rapid decrease of the resistance as a temperature was lowered [8]. In resonance type probes, usually one side of the sample coil is connected to a ground and another side is connected to a matching circuit, which transforms the resistive impedance of the sample coil to 50 Ω. Since the sample coil resistance (the resistance of Cu or Ag wires) changes rapidly at low temperature, it is often difficult to tune the resonance type probes. Haase et al. [9] mentioned another application of the transmission line probe to double resonance experiments, where two nuclei had close frequencies, although they wrote that their new double resonance probe could be retuned to a single resonance signal with a large line width.

In the present article, we constructed a transmission line NMR probe by using ceramic chip capacitors and performed intensive numerical calculations of the electrical characters based on the moment method, and compared them to those obtained by experiments. We derived a simple formula to predict the characteristic impedance and the cut-off frequency of any given geometry of the coil and the capacitance value. We also calculated the strength and the distribution of RF field inside the flat and the cylindrical coils. Detailed frequency dependences of these characters were simulated. The results were compared with the analytical formulae derived from the waveguide theory and with the results of the nutation experiments for various nuclei. A method to improve the sensitivity of the probe was proposed and also examined experimentally.

2. Method of simulation

2.1. π-Type transmission line probe

In the present work, we employed the model of the transmission line probe proposed by Lowe and Engelsberg [5] and Lowe and Whitson [7], which is shown in Fig. 1a. The circuits consist of $N\pi$ sections and each section contains a coil and two capacitors. Lowe and Engelsberg simplify the model by ignoring all the mutual inductances, so that the circuit is same as that of a N-cascaded low-pass filter. Subsequently, Lowe and Whitson improved the model by taking account of the mutual inductances between the neighboring sections. In our analyses we calculated all the self and mutual inductances explicitly for a given geometry of a coil, by using Neumann's formula.

The mutual inductance between the ith and jth coil sections is given by

$$M_{i,j} = (\mu_0/4\pi I_{Li} I_{Lj}) \int \mathrm{d}\vec{r}_i \int \mathrm{d}\vec{r}_j \left(\vec{J}(\vec{r}_i) \cdot \vec{J}(\vec{r}_j)/|\vec{r}_i - \vec{r}_j| \right), \tag{1}$$

where $\vec{r}_i$ and $\vec{r}_j$ are the coordinates of the ith and jth coil sections; $\vec{J}(\vec{r})$ and I_{Li} are the current density and the total current on the ith coil section, respectively. Analytical formulae can be derived for two filaments carrying current by using the integral formulae:

$$\int^x \mathrm{d}t/\sqrt{1+t^2} = \ln\left| x + \sqrt{1+x^2} \right|$$

and

$$\int^x t \ln f(t)\,\mathrm{d}t = \frac{1}{2}x^2 \ln f(x) - \int^x \frac{1}{2}t^2 \{ f'(t)/f(t) \}\,\mathrm{d}t.$$

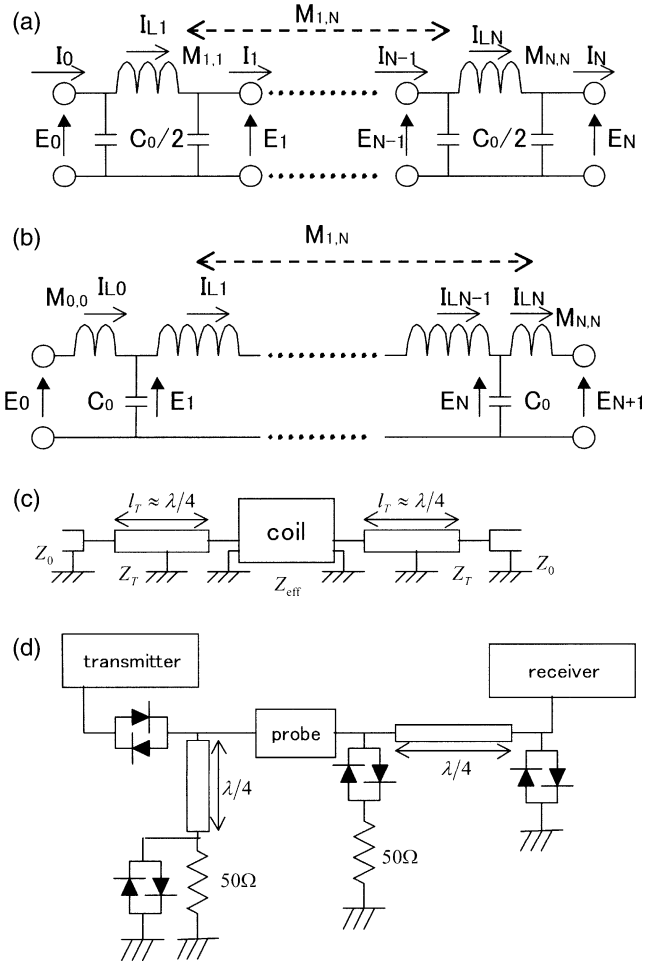

Fig. 1. Model circuits of a transmission line probe. (a) π-type transmission line probe. The circuit is consisted of N sections. Each section contains an inductor with a self-inductance M_{ii} and two capacitors with a capacitance $C_0/2$. There is a mutual inductance M_{ij} between the ith and jth coil sections. E_i and I_{Lk} denotes the voltage across the ith capacitor and the current on the kth coil, respectively. (b) T-type transmission line probe. Compared with (a), a half of inductor and a capacitor are removed from the last section and are inserted before the first section. (c) Impedance transformations by $\lambda/4$ cables. The transformer cables must have the characteristic impedance of $Z_T = \sqrt{Z_0 Z_{\text{eff}}}$, where Z_{eff} and $Z_0 = 50\,\Omega$ denotes the impedance of the transmission line coil and the feeding/receiving cables, respectively. (d) Experimental configurations. As described by Lowe and Engelsberg, a pair of crossdiodes and a $\lambda/4$ cable was employed for a RF switch operating between transmitting and detection modes.

We employed the formulae for two parallel and inclined filaments written in Grover's book [10]. Self-inductance was evaluated for a cylindrical wire by assuming RF current is distributed homogeneously on the surface of the wire. Eq. (1) reduces to

$$M_{i,i} \approx (\mu_0 l/2\pi)(\ln|2l/a| - 1), \tag{2}$$

where l and a are the length and the radius of the wire, respectively. Eq. (2) can be derived by using the formula, $\int_0^{\pi/2} \ln|\sin\theta|\,\mathrm{d}\theta = -(\pi/2)\ln 2$. It is worth to note that M_{ij} is negative when a pair of currents are flowing antiparallel to each other. When the number of turns was noninteger, the high frequency electrical characters of the coil were different from those of the coil with integer turns.

The current on each coil section was calculated by the Moments method [11–13]. We assumed that the displacement current $\vec{J}_{\text{D}} = \partial\vec{D}/\partial t$ is localized within capacitors. We ignored the capacitive couplings between coil sections, which may be important at high frequency, since the capacitance calculations are a little more involved. The moment method at first expresses a scalar (or vector) potential by a convolution integral of Green's function and a charge (or a current). The relations between currents and voltages (Kirchhoff's voltage law) are derived from these equations and the conservation law of a charge. The output voltage E_n and the current I_n on the nth section in Fig. 1a are given by:

$$E_{n-1} - E_n = RI_{Ln} + \mathrm{j}\omega\sum_{m=1}^{N} M_{nm}I_{Lm} \equiv \sum_{m=1}^{N} Z_{nm}I_{Lm}, \tag{3}$$

$$I_{n-1} - I_n = Y(E_n + E_{n-1}), \tag{4}$$

where R and $Y = (\mathrm{j}\omega C/2)$ are the resistance of a wire and the admittance of a capacitor, respectively [5,7]. The current on the nth coil is given by

$$I_{Ln} = I_n + YE_n. \tag{5}$$

Eqs. (3)–(5) are combined and rewritten into the following $2N$ dimensional linear equations:

$$\begin{bmatrix} \vec{E}_0^{(N)} \\ \vec{I}_0^{(N)} \end{bmatrix} = \begin{bmatrix} \hat{J} + \hat{Z}Y & \hat{Z} \\ Y\left(2\hat{1}^{(N)} + \hat{Z}Y\right) & \hat{J} + \hat{Z}Y \end{bmatrix} \begin{bmatrix} \vec{E}^{(N)} \\ \vec{I}^{(N)} \end{bmatrix} \equiv \hat{K}\begin{bmatrix} \vec{E}^{(N)} \\ \vec{I}^{(N)} \end{bmatrix}, \tag{6}$$

where the N-dimensional voltage and current vectors are given by

$$\vec{E}_0^{(N)} = \begin{bmatrix} E_0 \\ 0 \\ \vdots \\ 0 \end{bmatrix}, \quad \vec{I}_0^{(N)} = \begin{bmatrix} I_0 \\ 0 \\ \vdots \\ 0 \end{bmatrix}, \qquad \vec{E}^{(N)} = \begin{bmatrix} E_1 \\ E_2 \\ \vdots \\ E_N \end{bmatrix}, \quad \vec{I}^{(N)} = \begin{bmatrix} I_1 \\ I_2 \\ \vdots \\ I_N \end{bmatrix}. \tag{7}$$

$\hat{Z}$ is the impedance matrix given by Eq. (3). The N-dimensional matrices $\hat{J}$ and $\hat{1}^{(N)}$ are given by

$$\hat{J} = \begin{bmatrix} 1 & 0 & \cdots & 0 \\ -1 & 1 & \ddots & \vdots \\ 0 & \ddots & \ddots & 0 \\ 0 & 0 & -1 & 1 \end{bmatrix} \text{ and}$$

$$\hat{1}^{(N)} = \begin{bmatrix} 1 & 0 & \cdots & 0 \\ 0 & 1 & \ddots & \vdots \\ \vdots & \ddots & \ddots & 0 \\ 0 & \cdots & 0 & 1 \end{bmatrix}. \tag{8}$$

The four-terminal constants of the probe circuit are derived by inverting Eq. (6)

$$\begin{bmatrix} E_N \\ I_N \end{bmatrix} = \begin{bmatrix} A & -B \\ -C & A \end{bmatrix} \begin{bmatrix} E_0 \\ I_0 \end{bmatrix} = \begin{bmatrix} (\hat{K}^{-1})_{N,1} & (\hat{K}^{-1})_{N,N+1} \\ (\hat{K}^{-1})_{2N,1} & (\hat{K}^{-1})_{2N,N+1} \end{bmatrix} \begin{bmatrix} E_0 \\ I_0 \end{bmatrix}. \tag{9}$$

The circuit is passive and symmetric so that we employed $AD - BC = 1$ and $A = D$ in the above equation. The transmission line circuit is well characterized by a complex effective impedance $Z_{\text{eff}} = Z_{\text{eff, re}} + \mathrm{j}Z_{\text{eff, im}}$ and a propagation constant $\gamma = \alpha + \mathrm{j}\beta$, which are related to four terminal constants by the following equations:

$$Z_{\text{eff}} = \sqrt{B/C}, \tag{10}$$

$$\exp(\pm\gamma) = A \pm B/Z_{\text{eff}}. \tag{11}$$

The impedance matching requires $Z_{\text{eff}} = Z_0$, where Z_0 is characteristic impedance of a cable. The constants α and β are called as an attenuation constant and a phase constant, respectively. All of these three values are generally frequency dependent.

The input and output ports of the probe are usually connected to a voltage source V_{in} and to a load Z_0 (or a receiver), respectively, through cables of characteristic impedance Z_0. Since only the two travelling wave modes of

$$[\,E \quad I\,] = E[\,1 \quad \pm Z_0^{-1}\,]$$

are allowed in the cable, the continuity conditions of the voltage and the current determine the amplitudes of the reflected and the incident waves

$$V_{\text{in}}[\,1 \quad Z_0^{-1}\,] = V_{\text{in}}\{(Z_0 - Z_L)/(Z_0 + Z_L)\}[\,1 \quad -Z_0^{-1}\,] + V_{\text{in}}\{2Z_L/(Z_0 + Z_L)\}[\,1 \quad Z_L^{-1}\,]. \tag{12}$$

Z_L is the load impedance of the probe given by:

$$Z_L = (A + BZ_0^{-1})/(C + AZ_0^{-1}). \tag{13}$$

The incident voltage and current are calculated as

$$[\,E_0 \quad I_0\,] = 2Z_L V_{\text{in}}/(Z_0 + Z_L)[\,1 \quad Z_L^{-1}\,] = \{2V_{\text{in}}/(2A + BZ_0^{-1} + CZ_0)\} \times [\,A + BZ_0^{-1} \quad Z_0^{-1}(A + CZ_0)\,]. \tag{14}$$

The voltage reflection coefficient R and transmission coefficient T are given by:

$$R = (Z_L - Z_0)/(Z_L + Z_0) = (BZ_0^{-1} - CZ_0)/(2A + BZ_0^{-1} + CZ_0), \tag{15}$$

$$T = E_N/V_{\text{in}} = 2/(2A + BZ_0^{-1} + CZ_0). \tag{16}$$

By using Eqs. (5), (6), and (14), the current on the kth coil section I_{Lk} was calculated. The RF field due to I_{Lk} is obtained by integrating Ampère's formula for a straight filament,

$$\vec{B}_k(\vec{x}) = \{\mu_0(\vec{e}_\lambda \times \vec{e}_\rho)I_{Lk}/4\pi\rho\} \times \left\{ \left(\frac{1}{2}\lambda - x_\lambda\right) \Big/ \sqrt{\rho^2 + \left(\frac{1}{2}\lambda - x_\lambda\right)^2} + \left(\frac{1}{2}\lambda + x_\lambda\right) \Big/ \sqrt{\rho^2 + \left(\frac{1}{2}\lambda + x_\lambda\right)^2} \right\} \equiv \vec{g}_k\left(\vec{x}\right) I_{Lk}, \tag{17}$$

where λ and $\vec{e}_\lambda$ are the length and the unit vector parallel to the current, respectively. The coordinate $\vec{x}$ is measured from the midpoint of the filament. x_λ and ρ are given by $x_\lambda = \vec{x} \cdot \vec{e}_\lambda$ and $\rho\vec{e}_\rho = \vec{x} - \vec{e}_\lambda(\vec{e}_\lambda \cdot \vec{x})$, respectively.

Nuclear magnetization is affected only by the RF field rotating in the same direction as the Larmor precession. We assume that the static magnetic field is along the z-direction. The amplitudes $B_\pm$ and the phases $\phi_\pm$ of the rotating field are given by

$$B_\pm = \frac{1}{2}\sqrt{(B_x^c \pm B_y^s)^2 + (B_y^c \mp B_x^s)^2}, \tag{18}$$

$$\phi_\pm = \tan^{-1}\left(\frac{\pm B_y^c - B_x^s}{B_x^c \pm B_y^s}\right), \tag{19}$$

where the upper sign for the anti-clock wise rotating component. $B_\alpha^{c,s}$ $\alpha = x, y$ denotes the magnetic field components oscillating in the same phase (c) and in the phase delayed by 90° (s) from the complex input voltage V_{in}, respectively. These are calculated by

$$B_\alpha^c(\vec{x}) = \sum_{k=1}^{N} g_{\alpha,k}(\vec{x})\mathrm{Re}\{I_{Lk}\} \tag{20}$$

and

$$B^s_{\alpha,k}(\vec{x}) = \sum_{k=1}^{N} g_\alpha(\vec{x})\mathrm{Im}\{I_{Lk}\}, \tag{21}$$

respectively.

2.2. T-type transmission line probe

We also employed the T-type circuit shown in Fig. 1b for the simulation. The self-inductances or the number of turns at both the ends are the half of the other sections. The procedure of the calculation is similar to that employed for the π-type circuit. Here we will show only the results of the calculation. The four terminal constants are defined by

$$\begin{bmatrix} E_0 \\ I_{L,0} \end{bmatrix} = \begin{bmatrix} A & B \\ C & A \end{bmatrix} \begin{bmatrix} E_{N+1} \\ I_{L,N} \end{bmatrix}. \tag{22}$$

These three constants were calculated as follows:

$$A = (1 + 2YZ_{00} - \Theta_{11})/(\Theta_{12} - 2YZ_{N0}), \tag{23}$$

$$B = (1 + 2YZ_{00} - \Theta_{11})^2/Y(\Theta_{12} - 2YZ_{N0}) - (\Theta_{12} - 2YZ_{N0})/Y, \tag{24}$$

$$C = Y/(\Theta_{12} - 2YZ_{N0}). \tag{25}$$

The impedance matrix $\hat{Z}$ is given by Eq. (3), however it has $(N+1)^2$ elements numbered from 0 to N. To calculate Θ_{11} and Θ_{12}, we define the following $(N-1)\times(N-1)$ matrix $\hat{\Xi}$ from 1st to $(N-1)$th rows and columns of $\hat{Z}$

$$\hat{\Xi} = \begin{bmatrix} 2+2YZ_{1,1} & -1+2YZ_{1,2} & \cdots & 2YZ_{1,N-1} \\ -1+2YZ_{2,1} & 2+2YZ_{2,2} & \ddots & \vdots \\ 2YZ_{3,1} & \ddots & \ddots & -1+2YZ_{N-2,N-1} \\ \vdots & \cdots & -1+2YZ_{N-1,N-2} & 2+2YZ_{N-1,N-1} \end{bmatrix}. \tag{26}$$

We also define the $N-1$ dimensional vectors

$${}^t\vec{b}_0 = [1 - 2YZ_{0,1}, -2YZ_{0,2}, \ldots, -2YZ_{0,N-1}] \tag{27}$$

and

$${}^t\vec{b}_N = [-2YZ_{N,1}, \ldots, -2YZ_{N,N-2}, 1 - 2YZ_{N,N-1}]. \tag{28}$$

Θ_{11} and Θ_{12} in Eqs. (23)–(25) are given by:

$$\Theta_{11} = {}^t\vec{b}_0\hat{\Xi}^{-1}\vec{b}_0, \tag{29}$$

$$\Theta_{12} = {}^t\vec{b}_0\hat{\Xi}^{-1}\vec{b}_N. \tag{30}$$

The voltage reflection and transmission coefficients are calculated by Eqs. (15) and (16). Then the currents on the 0th and the Nth coils are determined for a given input voltage V_{in} by using Eq. (22) and $E_{N+1} = I_{L,N}Z_0 = TV_{\mathrm{in}}$. They are used to calculate the currents on the other coil sections given by

$$\vec{I}_L^{(1,N-1)} = I_{L,0}\hat{\Xi}^{-1}\vec{b}_0 + I_{L,N}\hat{\Xi}^{-1}\vec{b}_N. \tag{31}$$

3. Experiments

The coils were made by using an AWG30 Teflon covered wire (the conductor diameter 0.26 mm, Teflon wrapping diameter 0.56 mm) and chip capacitors. (Murata GRH111CH060D500PB: 6pF, GHM1038SL 560J3k: 56pF, etc. A typical size was a 2.8 mm cube.) Nonmagnetic chip capacitors with the similar size are available from American technical Ceramics (www. atceramics.com). At first, Teflon wrappings were separated from inner conductors. Two conductor wires and a Teflon tube from the wrapping were wound onto a shaft of a 2.5 mm diameter drill. A thin paper was wrapped around the shaft, so that the coil was easily removed from the shaft after it was fixed by epoxy glue. A caution was made by a reviewer that Epoxy had been known to reduce the Q of resonant type of coils. However, we did not detect any serious effect. It might appear when the length coil is very long. The Teflon tube works as an insulator between the neighboring turns of the conductor wires. The pitches of the coils made in this manner were always very close to 1.2 mm. Two mm wide capacitor leads were cut from a 0.1 mm thick copper film, and were soldered to the conductor wires and to the chip capacitors at every n_c turn. n_c was either 3 or 1.5, while the total number of the capacitors was 5 or 11, respectively. The length of the capacitor lead was around 2 mm. It was made the shortest to minimize the self-inductance. The other sides of the capacitors were grounded to a copper film.

The reflection and the transmission of the probe were measured by an Agilent Technologies' network analyzer, 8712ES. NMR experiments were performed on a Bruker DSL400 spectrometer. The circuit used was similar to Fig. 4 of the paper by Lowe and Engelsberg [5] and reproduced in Fig. 1d. Almost the same signal was obtained, when we omitted the diode boxes and the $\lambda/4$ cables in the transmitter side and connected the transmitter directly to one of ports of the probe. A concen-

trated water solution of NaBr was used for the measurements of ^{23}Na, ^{79}Br, and ^{1}H, while a solution of K_2PtCl_6 was employed for ^{195}Pt.

4. Results and discussions

4.1. Simulation of electrical characteristics of a flat coil

At first, we consider the flat coil transmission line probe, whose geometry is given in Fig. 2. Here the pitch is assumed to be constant, i.e., $p(k) = p$ for $k = 1, \ldots, N_t$, where N_t is the total number of turns. The capacitance C_0 was the only variable and was adjusted so that the real part of the effective impedance matches with the cable impedance of 50 Ω at the lowest frequency. The number of turns between capacitors n_c was varied while the dimensions of the coil and the total number of turns N_t were fixed.

The propagation constants, the effective impedance and the magnitudes of reflection and transmission were calculated as a function of a frequency. The results are shown in Fig. 3. The frequency dependences of these electrical characteristics are similar to those of a N-cascaded LC low-pass filter, where mutual inductances between different π-sections are made zero in Fig. 1a. There is a cut-off frequency v_c above which the attenuation constant α deviates from zero. The cut-off frequencies in Fig. 3 are 1160, 480, and 200 MHz for $n_c = 1, 2$, and 4, respectively. Above the cut-off frequency, the magnitude of transmission falls to zero, while the magnitude of reflection becomes a unity, so that the entire incident wave is reflected. The phase constant β increases almost linearly with v when $v \ll v_c$. It rises steeply near v_c and becomes $N\pi = N_t\pi/n_c$ at v_c. The slope of β vs. frequency is almost independent

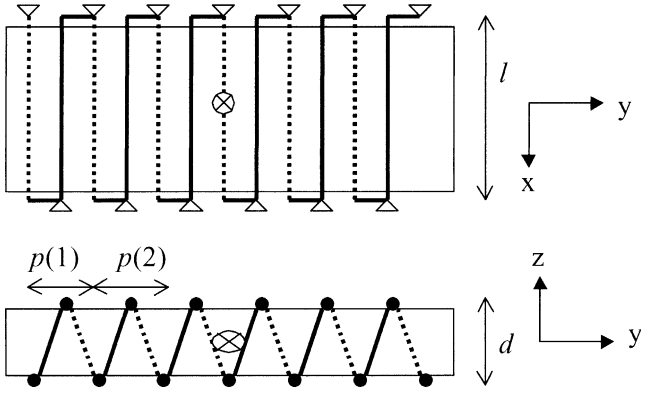

Fig. 2. Geometry and dimensions of the flat transmission line coil. The origin is chosen at the center of the coil and indicated by ⊗. The pitch $p(k)$ is defined for each turn, $k = 1, \ldots, N_t$, where N_t is the number of turns. The triangles indicate the positions of capacitors. Capacitors of $1/2C_0$ are attached at the first and the last triangles and are terminated to the ground. The capacitors of C_0 are connected at every n_c turns between the both ends.

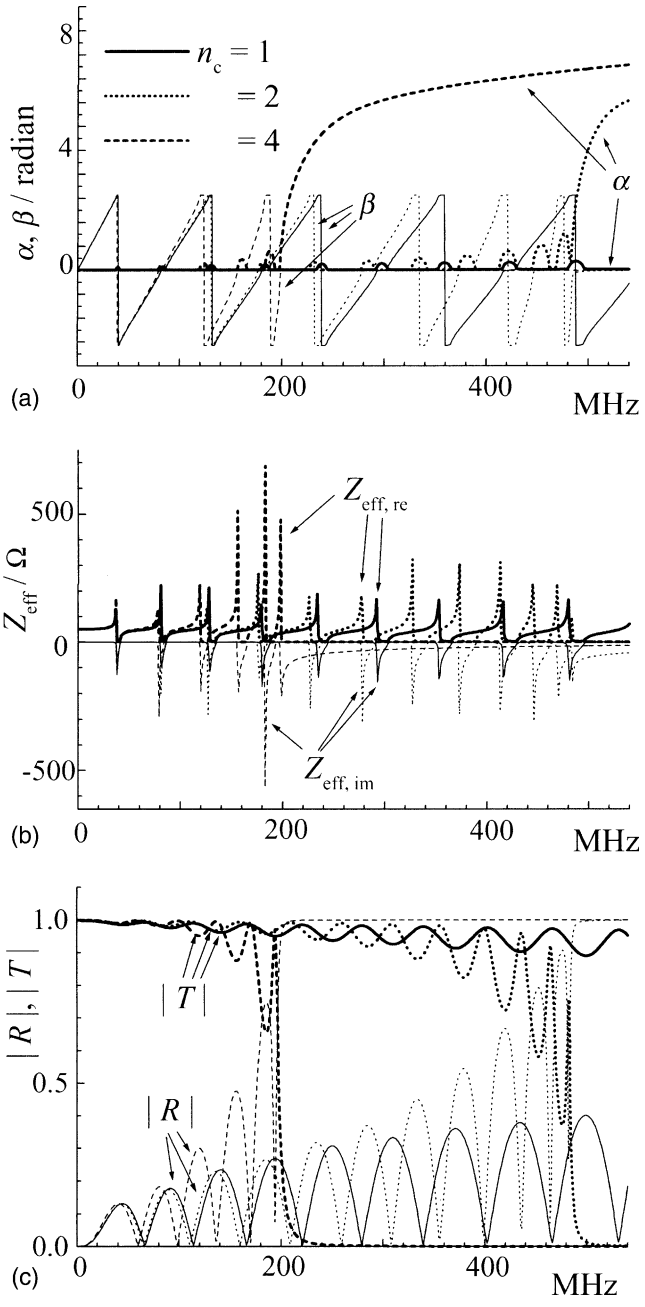

Fig. 3. Simulated electrical characteristics of flat transmission line coils. Frequency dependences of a propagation constant $\gamma = \alpha + j\beta$ (a), effective impedance $Z_{eff} = Z_{eff,re} + jZ_{eff,im}$ (b) an absolute reflection $|R|$ and an absolute transmission $|T|$ (c) were calculated for the three n_c values. The dimensions of the coil are $l = 9$ mm, $d = 2.3$ mm, $p = 1.2$ mm, and $N_t = 24$. The capacitance C_0 was determined from the condition $Z_{eff}(v \approx 0) = 50\,\Omega$ and was 11.1, 22.1, and 44.2 pF for $n_c = 1$, 2, and 4, respectively.

of n_c as long as $v \ll v_c$ and when N_t is constant. When N_t was doubled, β also became doubled, which indicates that the phase delay β through the coil is proportional to the coil length.

The difference from the low-pass filter circuit is that Z_{eff} shows peaks at the frequencies where β becomes an integer multiple of π, i.e., $\beta = k\pi$, $k = 1, 2, \ldots, N - 1$. At

these frequencies v_k, α becomes nonzero and positive and the magnitude of reflection takes maxima. Another marked difference is that the currents $I_{L,k}$ on different coil sections are not uniform. The phase of the current varies linearly as a function of position k. However, the magnitude of the current shows a sinusoidal oscillation as a function of k as shown in Fig. 4b. It can be understood as a standing wave of current within the transmission line probe. If there is only the wave travelling in one direction, the amplitude of current must be uniform over all the k values. Since the boundary condition $I_N = Z_0^{-1}E_N$ must be satisfied, the phase of the current oscillation is fixed near 0° at the last coil section ($k = 24$), while the amplitude of the current is close to $Z_0^{-1} = (1/50\,\Omega) = 20\,\mathrm{A\,(kV)^{-1}}$ as shown in Fig. 4a. The undulation of the current $|I_{L,k}|$ over k increases monotonously as the carrier frequency increases as shown in Fig. 4a. When the oscillation of the current amplitude is large, the RF magnetic field in the transmission line probe also oscillates along the y-axis, thus the RF field becomes very inhomogeneous.

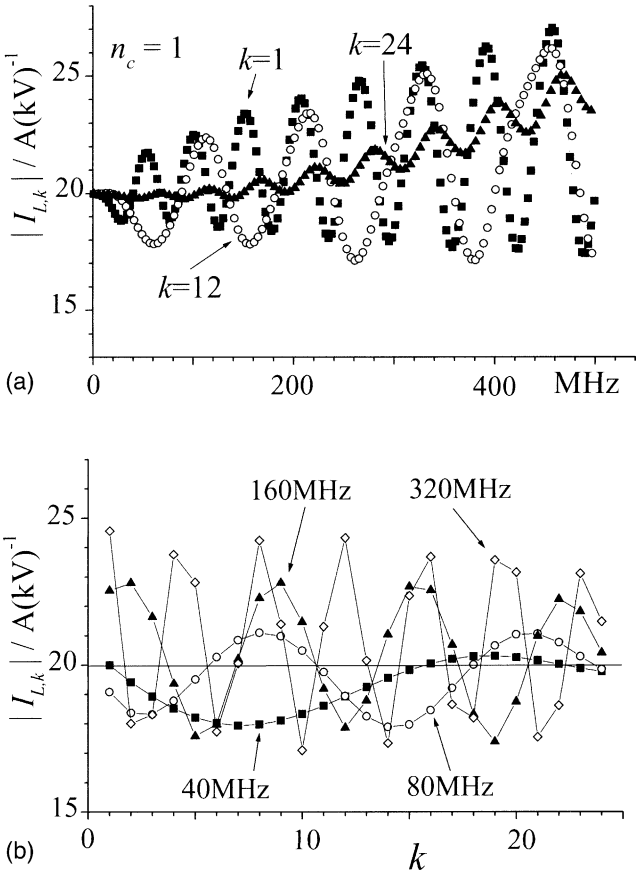

Fig. 4. Magnitude of the calculated current $|I_{L,k}|$ on the kth coil section of a flat transmission line coil. The currents are shown for a unit input voltage. The dimensions of the coil are the same as Fig. 3. n_c and N_t are 1 and 24, respectively. (a) and (b) are the frequency and the position dependences, respectively. The currents oscillate around $Z_{\mathrm{eff}}^{-1} = 50\,\Omega^{-1} = 20\,\mathrm{A\,(kV)^{-1}}$, which shows the occurrence of a standing wave within the coil.

4.2. Approximate formulae for the electrical characteristics

It is convenient if one can relate dimensions of a coil to its electrical properties like $Z_{\mathrm{eff}}(0)$, v_c, and v_k by using the approximate formulae without any explicit numerical calculations. An analytical solution exists for an N-cascaded low-pass filter circuit, where each section is independent. We assume that the total inductance of a coil is distributed to the $N = (N_t/n_c)$ independent coil sections. According to this model, the self-inductance is given by $M_{j,k} = \delta_{j,k} n_c \bar{M}$, where $\bar{M}$ is the total inductance of a coil divided by the number of turns, N_t. According to this model the effective impedance at $v = 0$ is given by

$$Z_{\mathrm{eff}}(0) = \sqrt{n_c \bar{M}/C_0}. \tag{32}$$

The circuit is characterized by a cut-off frequency v_c, which is given by

$$v_c = 1/\pi\sqrt{n_c \bar{M} C_0} = Z_{\mathrm{eff}}(0)/\left(\pi n_c \bar{M}\right). \tag{33}$$

The phase constant β for the whole length of the probe is given by the following equation under the condition $v \ll v_c$:

$$\beta = 2N \sin^{-1}(v/v_c) \approx 2Nv/v_c. \tag{34}$$

v_k is derived by setting $\beta = k\pi$

$$v_k = \frac{1}{2} k\pi (n_c v_c/N_t). \tag{35}$$

When the above equation is combined with Eq. (33), v_k does not depend on n_c. The attenuation constant α is given by

$$\alpha = 2N \cosh^{-1}(v/v_c), \tag{36}$$

under the condition of $v \geqslant v_c$. The above equation shows the transmission vanishes rapidly $v \approx v_c$.

Now we will estimate $Z_{\mathrm{eff}}(0)$, v_c, and v_1 for the flat coil probes with the dimensions given in Fig. 3 ($l = 9\,\mathrm{mm}$, $d = 2.3\,\mathrm{mm}$, $p = 1.2\,\mathrm{mm}$, $N_t = 24$) by using the above formulae and compare them to the values obtained from the simulation. At first, $\bar{M}$ was calculated to be 27.6 nH by using

$$\bar{M} = N_t^{-1} \sum_{i,j=1}^{N} M_{i,j}, \tag{37}$$

where $M_{i,j}$ were obtained by using Neumann's formula. Another simpler estimate was made from the following formula of inductance for an infinitively long coil

$$\bar{M} = S\mu_0/p. \tag{38}$$

$S = ld$ is a crosssection of a flat coil. The coil dimensions in Fig. 3 gave $\bar{M} = 21.7\,\mathrm{nH}$.

If we used $\bar{M} = 27.6\,\mathrm{nH}$ and calculated C_0 from Eq. (32) together with the matching condition, $Z_{\mathrm{eff}}(0) = 50.0\,\Omega$, these values of C_0 agreed with that obtained from

the simulation within 1%. While formula (38) provided the 20% smaller values. v_c and v_1 were calculated by the first method to be $(576/n_c)$ MHz and 38 MHz, respectively. The second method provided $(733/n_c)$ MHz and 48 MHz. The corresponding values obtained from the simulation were $(800–1160)/n_c$ MHz and 39 MHz, respectively. The first method provided better estimate of v_1 than the second method. But both the methods provided much smaller values of v_c than the simulation.

4.3. RF field homogeneity of a flat coil

According to the above model of the independent N-cascaded π-sections, the currents flowing through the neighboring sections have a phase delay given by $\beta/N = 2\sin^{-1}(v/v_c)$. As the carrier frequency increases, this phase delay increases and becomes 180° at v_c. The RF magnetic fields produced by the different π-sections interfere more destructively as the carrier frequency increases. Lowe and Whitson [7] derived the following formula for the rotating magnetic field inside the flat coil at $|z| \ll d$. They assumed that the coil extended along the x- and y-axes to infinity, i.e., $l \to \infty$ and $N_t \to \infty$ in Fig. 2 and that the instantaneous current along the $+x$ $(-x)$ direction was distributed on the plane $z = +\frac{1}{2}d$ $(z = -\frac{1}{2}d)$ with the density $\frac{1}{2}(I/p)\exp\{i(\kappa y - \omega t)\}$. The factor $\frac{1}{2}$ arises from the fact that the current contains the minus frequency component which does not resonate with the nuclear spins. The magnitude of the rotating magnetic field was given by

$$|B_+| = |B_y| = \frac{1}{2}\mu_0(I/p)\exp(-\kappa d/2)\cosh(\kappa z). \tag{39}$$

Since κp is the phase delay per turn, it is equal to the phase constant divided by the number of turns, β/N_t. If we employ again the circuit of low-pass filter, κ can be rewritten as $\kappa = v/(n_c p v_c)$. The current I is approximately given by $I \approx V_{in}/Z_0$ as shown in Section 4.1. The rotating field at the center of the coil is given by

$$|B_+| = \frac{1}{2}\mu_0(V_{in}/Z_0 p)\exp(-v/v_d), \tag{40}$$

where the decay constant v_d is given by

$$v_d = (2n_c p v_c/d) = \{2Z_{eff}(0)/\pi\bar{M}\}(p/d) \approx (2Z_0/\pi\mu_0 l)(p/d)^2. \tag{41}$$

For the flat coil with the dimensions given in Fig. 3, $v_d = 615$ MHz and $(\mu_0/2Z_0 p) = 10.47\,\text{mT (kV)}^{-1}$ were calculated.

Fig. 5a shows the rotating field at the center of the coil obtained from the numerical calculations in comparison with the value calculated from approximate Eq. (40). The numerical results show the oscillating decays, however, the upper traces of the oscillations coincide with the exponential curve obtained from Eq. (40). Thus Eq. (40) provides a quick estimate for the $|B_+|$ values

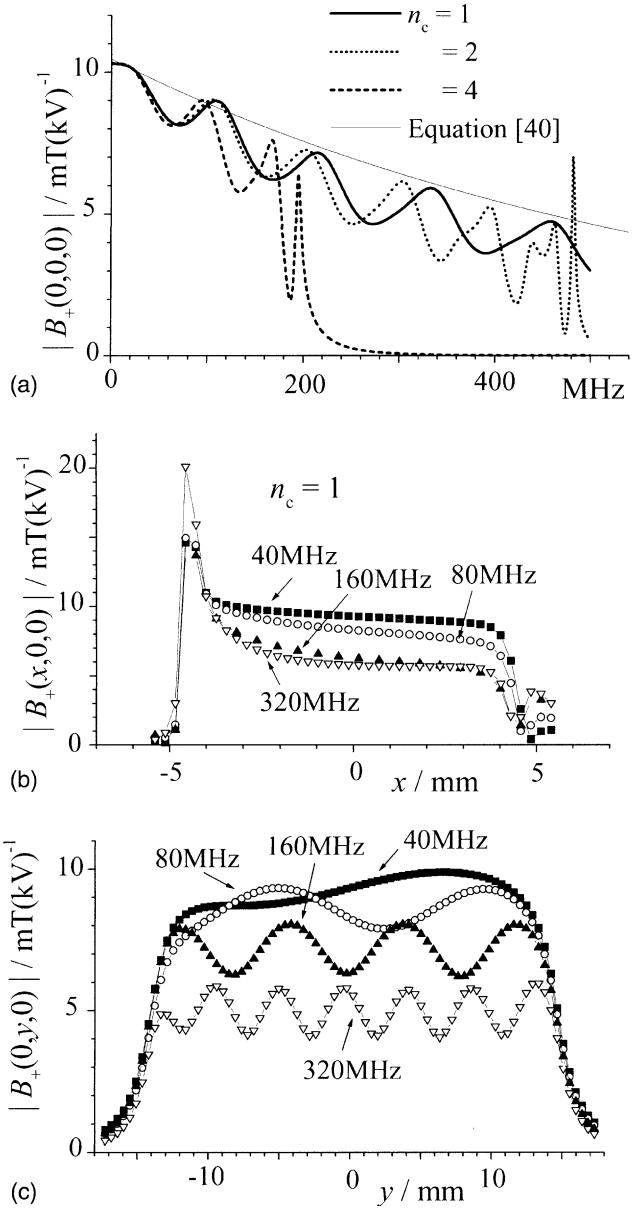

Fig. 5. Simulated variations of absolute rotating magnetic field $|B_+(x,y,z)|$ of flat transmission line coils against carrier frequency and at the coil center (a), against x along $y = 0$ (b), and against y along $x = 0$ (c). The dimensions of a flat coil are the same as those of Fig. 3. The solid, the broken, and the dotted thick lines in (a) shows the simulated curves for $n_c = 1$, 2, and 4, respectively. The thin line was calculated from Eq. (40). It agrees with the simulated curves at maxima. All the results in (b) and (c) were calculated for $n_c = 1$.

when a new transmission line probe is constructed. The oscillatory behaviors of the simulated curves are apparently due to the standing wave of the current amplitudes over the different coil sections as explained in Fig. 4.

The field distributions along the x- and y-axes were calculated and are shown in Figs. 5b and c, respectively. As expected from the undulation of the current amplitude over the different coil sections, the field also

oscillates as a function of y. The resulting inhomogeneity of the field is around 17% for the region $|y| < 10$ mm and at the carrier frequency 80 MHz. The inhomogeneity increases as the frequency increases and becomes 37% at the frequency 320 MHz. Along the x-axis the magnetic field changes very rapidly only near the wires at $x = \pm 4.5$ mm. From Ampère's law the magnetic field close to a single wire is expected to diverge by $1/r$, where r is the distance from the wire. The same type of the divergence is observed near the wires at $z = \pm 1.15$ mm. If we employ a flat cable instead of a line to wind the coil, the divergence will be reduced. In the central region with $|x| < 2$ mm the field decreases monotonously and varies 13% at 80 MHz as the x-coordinate increases.

Instead of examining the field near the flat cable, let us consider here the continuously distributed current on a conductor plane at $x = \pm l/2$ and investigate the RF field near its surface. The model of Lowe and Whitson [7] can be used by exchanging the x- and z-axes and by making $d \to \infty$. The observation point is so close to the conductor plane at $x = l/2$ or $-l/2$, that current flowing on that plane dominantly produces the RF field. The x-component of the field becomes

$$B_x = -\frac{1}{2} i\mu_0 (I/p) \exp(-\kappa l/2) \sinh(\kappa x), \tag{42}$$

while the y-component is still given by Eq. (39). The rotating field is given by

$$|B_+| = |B_x + iB_y| = \frac{1}{2}\mu_0 (I/p) \exp(-\kappa l/2) \exp(-\kappa x). \tag{43}$$

The sign of κ is reversed for the travelling wave in the opposite direction. Eq. (39) or (43) does not show any divergence of RF field near the coil surface at $z = \pm d/2$ and $x = \pm l/2$, respectively. The field homogeneity along the x and the z directions may be improved by using a flat cable instead of a cylindrical cable to wind the coil. The homogeneity along the z-axis is estimated by $\cosh(\kappa z)$ or $\exp(\pm\kappa z)$, where $|\kappa z| \leqslant \kappa d/2 = v/v_d$. Since the condition $v \ll v_d$ must be satisfied to obtain the enough strength of RF field, $|\kappa z| \ll 1$ is always fulfilled. The RF field homogeneity in the xz plane may not be so severe if the flat cable is used to wind the coil.

4.4. Improvement of field homogeneity by a variable pitch flat coil

However, to reduce the inhomogeneity along the y-direction we have to change the electrical characteristics of the probe circuit and have to reduce the oscillation of the current over different coil sections. It can be achieved by varying the pitch over the coil. Since the coil at the ends have only a neighboring loop, the sum of inductance $\sum_{j=1}^{N} M_{i,j}$ for a particular wire i becomes smaller near the ends than that at the center. We considered that the reflection was caused by this distribution of inductance, so that we made the pitch near the ends smaller than that at the center to increase the inductance. We varied the pitch according to the following equation:

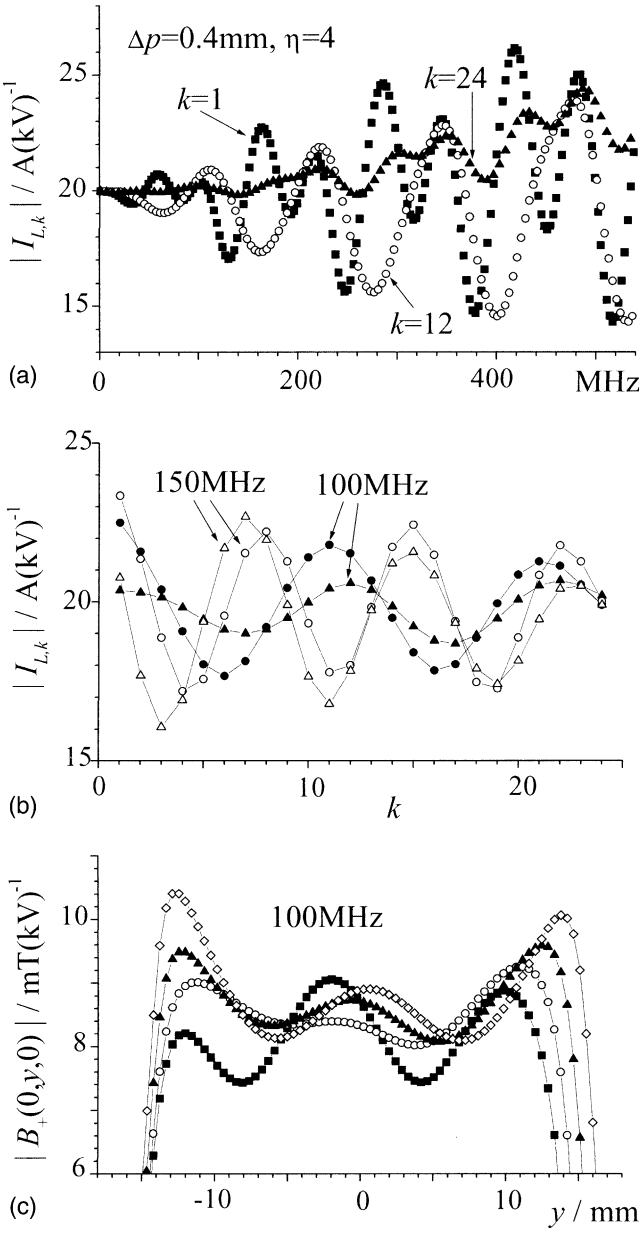

Fig. 6. Simulations of variable pitch flat transmission line coils. The dimensions of the coil are $d = 2.3$ mm, $l = 9$ mm, $p_c = 1.2$ mm, $N_t = 24$, $n_c = 1$, and $\eta = 4$. The magnitudes of currents $|I_{L,k}|$ of the different kth coil sections were calculated as a function of a frequency in (a) or as a function of k at 100 and 150 MHz in (b). If (a) is compared with Fig. 4a, it is apparent that the amplitudes of standing waves are suppressed below 100 MHz. The circles and the triangles in (b) were calculated for Δp 0.0 and 0.4 mm, respectively. The y dependences of magnitudes of rotating fields are shown in (c), when Δp is varied as 0 (■), 0.2 (○), 0.4 (▲), and 0.6 mm (◇). C_0 was determined from the impedance matching condition and was 11, 9.5, 9.6, and 9.9 pF, for $\Delta p = 0.0$, 0.2, 0.4 and 0.6 mm, respectively.

$$p(i) = p_c - \Delta p|(N_t + 1 - 2i)/(N_t - 1)|^{\eta}, \quad i = 1, \ldots, N_t. \tag{44}$$

The pitch at the center $i = (N_t + 1)/2$ is given by p_c, while those at the ends become $p_c - \Delta p$. We fixed $p_c = 1.2$ mm and adjusted the positive parameters Δp and η in order to obtain the best homogeneity.

Fig. 6a shows the frequency dependence of the current amplitudes for the coil with $\Delta p = 0.4$ mm and $\eta = 4$. The magnitudes of the currents are almost constant below 120 MHz. When we look at the k-dependence in Fig. 6b, the amplitude of the oscillation is reduced at 100 MHz by increasing Δp from 0 to 0.4 mm. However, at 150 MHz the amplitude of $\Delta p = 0.4$ mm is slightly larger that of $\Delta p = 0$. The variable pitch approach can improve the field homogeneity for the frequency below 120 MHz. The magnitude of the rotating field was calculated as a function of y at 100 MHz for the Δp values from 0 to 0.6 mm and is shown in Fig. 6c. As Δp increased, the field near the ends of the coil increased, while the oscillation near the center was minimized for $\Delta p = 0.2$ and 0.4 mm. The best homogeneity was achieved for $\Delta p = 0.4$ mm and $\eta = 4$. The inhomogeneity in the region of $|y| < 10$ mm was 10%, while that of the constant pitch coil was 20%.

4.5. RF field homogeneity of a cylindrical coil

In the first paper, Lowe and Engelsberg [5] made a cylindrical coil transmission line probe. In the second paper, Lowe and Whitson [7] mentioned the cylindrical coil have two problems; the very inhomogeneous RF field and the difficulty of the construction. The second problem is now solved because the commercial chip capacitors are available. We will show here that the RF field homogeneity of a cylindrical coil is comparable to that of a flat coil, if the diameter of the coil is as small as the thickness of a flat coil d.

We consider an infinitely long cylindrical coil which extends along the y-axis and has a radius a and a pitch p. In the same manner as the flat coil of Fig. 2, a capacitor C_0 is connected at every n_c turns. We approximate the cylindrical coil by a cylinder having a travelling wave of current on its surface given by

$$\begin{aligned} d\vec{I}(y,\phi) &= \rho_I(y)\, d\vec{l}(\phi) \\ &= (I_{max}/2p)\exp\{i(\kappa y - \omega t)\} a\, d\phi(\cos\psi \vec{e}_\phi \\ &\quad + \sin\psi \vec{e}_y), \end{aligned} \tag{45}$$

where ψ is the pitch angle given by

$$\tan\psi = p/2\pi a. \tag{46}$$

$(\vec{e}_\rho, \vec{e}_\phi, \vec{e}_y)$ are unit vectors along cylindrical coordinates. The magnetic field at the center of the coil can be easily calculated from Ampère's law

$$\vec{B}(0,0,0) = \left(\frac{\mu_0}{4\pi}\right)\int_{-\infty}^{\infty} dy \int_{\phi=0}^{\phi=2\pi} \frac{\rho_I d\vec{l} \times (-\vec{R})}{R^3}, \tag{47}$$

where $\vec{R}$ is the vector from the origin to a point on the cylinder surface

$$\vec{R} = y\vec{e}_y + a\vec{e}_\rho. \tag{48}$$

After integrating over ϕ, only the y-component remains.

$$\begin{aligned} B_y(0,0,0) &= \frac{\mu_0 I\cos\psi}{2p}\int_0^{\infty} dy \frac{a^2\cos(\kappa y)}{(a^2+y^2)^{3/2}} \\ &= \frac{\mu_0 I\cos\psi}{2p}\frac{d}{da}\boldsymbol{K}_0(\kappa a) \\ &= \frac{\mu_0 V_{in}\cos\psi}{2Z_0 p}(\kappa a)\boldsymbol{K}_1(\kappa a), \end{aligned} \tag{49}$$

where $\boldsymbol{K}_1$ is the modified Bessel function of the second kind. $x\boldsymbol{K}_1(x)$ is a unity at $x = 0$ and decreases monotonically as x increases. κ can be estimated by using a circuit of an N-cascaded low-pass filter in the same manner as we derived Eq. (41). Here we replace κa by v/v_d^{cylinder}, where

$$v_d^{\text{cylinder}} = (Z_0/\pi^2\mu_0 a)(p/a)^2. \tag{50}$$

There is another method calculating the field distribution inside the cylindrical coil. That is the waveguide theory applied to travelling wave tubes [2,14]. The waveguide theory showed that there are only two independent field components $E_y(\rho,\phi)\exp i(\kappa y - \omega t)$ and $B_y(\rho,\phi)\exp i(\kappa y - \omega t)$ and the other four amplitudes $E_\rho(\rho,\phi)$, $E_\phi(\rho,\phi)$, $B_\rho(\rho,\phi)$, and $B_\phi(\rho,\phi)$ are derived from Maxwell equations for vacuum. The fields inside and outside the cylinder are proportional to the first and the second kind modified Bessel functions, $\boldsymbol{I}_0(\tau\rho)$ and $\boldsymbol{K}_0(\tau\rho)$, respectively. τ is related to the wave number κ by $\tau = \sqrt{\kappa^2 - (2\pi v/c)^2}$. Since the phase velocity of a travelling wave in the transmission line is much smaller than the light velocity in vacuum, one can approximate $\tau \approx \kappa$.

The amplitudes $E_y(\rho,\phi)$ and $B_y(\rho,\phi)$ are given by

$$(E,B)_y(\rho,\phi) = \begin{cases} (\boldsymbol{A},\boldsymbol{B})_1\boldsymbol{I}_0(\kappa\rho), & \rho < a, \\ (\boldsymbol{A},\boldsymbol{B})_2\boldsymbol{K}_0(\kappa\rho), & \rho > a \end{cases}. \tag{51}$$

The four coefficients $\boldsymbol{A}_1$, $\boldsymbol{A}_2$, $\boldsymbol{B}_1$, and $\boldsymbol{B}_2$ are determined from the following boundary conditions: (i) The electric field component parallel to the wires is zero on the inner and (ii) on the outer cylinder surface. (iii) The electric field component perpendicular to the wires and on the cylinder surface varies continuously across the cylinder surface. (iv) The magnetic field component perpendicular to the wires and on the cylinder surface jumps by the current density multiplied by μ_0 across the cylinder surface. These four conditions determine the four amplitude coefficients. In the theory of travelling wave tubes there is one more boundary condition that is the

continuity of the magnetic field parallel to the wires across the cylinder surface. However, in the present case there are capacitors attached outside the cylinder and there are the displacement current perpendicular to the cylinder and the currents through the ground loops, which produces the extra magnetic field parallel to the wires and outside the cylinder.

By using these boundary conditions, we obtained the magnetic field inside the cylinder

$$B_y(\rho,0,0) = (\mu_0 V_{\text{in}} \cos\psi/2Z_0 p)(\kappa a)\boldsymbol{K}_1(\kappa a)\boldsymbol{I}_0(\kappa\rho), \quad (52)$$

$$B_\rho(\rho,0,0) = \mathrm{j}(\mu_0 V_{\text{in}} \cos\psi/2Z_0 p)(\kappa a)\boldsymbol{K}_1(\kappa a)\boldsymbol{I}_1(\kappa\rho). \quad (53)$$

The rotating magnetic field inside the cylinder is given by

$$\begin{aligned} B_+(\rho,\phi,0) &= B_y(\rho,0,0) - \mathrm{j}B_x(\rho,0,0)\sin\phi \\ &= (\mu_0 V_{\text{in}} \cos\psi/2Z_0 p)(\kappa a)\boldsymbol{K}_1(\kappa a)\{\boldsymbol{I}_0(\kappa\rho) \\ &\quad + \boldsymbol{I}_1(\kappa\rho)\sin\phi\}. \end{aligned} \quad (54)$$

Since Eq. (54) is real, the phase of a RF magnetic field is constant over the plane perpendicular to the y-axis. The function $(v/v_{\text{d}})\boldsymbol{K}_1(v/v_{\text{d}})$ decays monotonically as the carrier frequency increases. The asymptotic form for the large v is $\sqrt{\pi v/2v_{\text{d}}}\exp(-v/v_{\text{d}})$, so that the decay is slightly slower than the exponential. The good homogeneity of the RF field in the xz plane is obtained as long as $\kappa\rho \ll 1$. It is always satisfied under the condition $v/v_{\text{d}} \ll 1$, which is necessary for the RF field to be strong enough, since $\kappa\rho < \kappa a = v/v_{\text{d}}$. The field inhomogeneity in the xz-plane is not serious for a cylindrical coil if the continuous distribution of the current is assumed.

4.6. Comparisons between experiments and simulations of cylindrical coils

We made the cylindrical transmission line probe as described in the experimental section. The simulation was performed for the same dimensions of the coil by using the T-type circuit shown in Fig. 1b. It was uncertain whether the simulations and the experiments agreed or not, because the effects of the ground loops were ignored in the simulations and because the real coils constructed could include some imperfections. At first, we compare the calculated and the experimental results of the absolute transmissions and reflections in Fig. 7. When the dimensions of the coil is fixed, C_0 is only a variable. In (a) and (b), C_0 was varied around the impedance matching condition, $Z_{\text{eff}}(v=0) = 50\,\Omega$, which was determined to be $C_0 = 8.84\,\text{pF}$ by the simulation.

From the comparisons between (a) and (b), the cut-off frequencies of the experimental probes are 80% of the

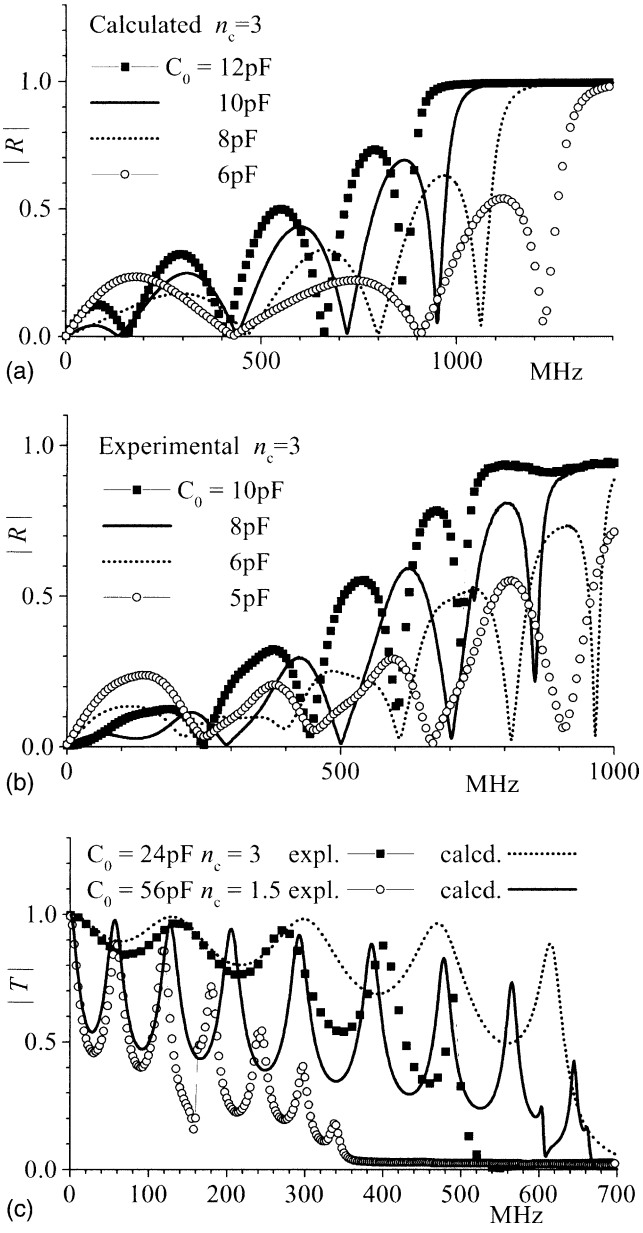

Fig. 7. Comparisons between calculated and experimental absolute reflections $|R|$ and transmissions $|T|$ of cylindrical transmission line coils. The diameter and the pitch of the coil were 1.35 and 1.2 mm, respectively. The both ends of the coil were terminated by the $n_c/2$ turns (T-type circuit of Fig. 1b). The total number of the capacitors is 5 for $n_c = 3$ and 11 for $n_c = 1.5$. The absolute reflections $|R|$ were calculated for the capacitor value C_0 from 6 to 12 pF, and are shown in (a). The experimental absolute reflections are shown in (b). In (c), we compare the experimental and the calculated absolute transmissions $|T|$ of the two low-impedance coils: 30.4 Ω for $C_0 = 24\,\text{pF}$ and 14.2 Ω for $C_0 = 56\,\text{pF}$. They were connected to 50 Ω cables and a terminator. Numbers of the maxima of $|R|$ are not the same between (a) and (b). Figure (c) shows better agreements between the experimental and simulated curves.

simulated probes. It was found experimentally that the shape of the ground affected the cut-off frequencies or the reflections at high frequencies. The largest cut-off frequency was obtained experimentally at a given C_0

value, when the capacitors were connected directly to a large ground conductor. The capacitor leads connected to the coil were made as short and wide as possible so that the inductances of the leads could be minimized. The reflection in the low-frequency region became the smallest at $C_0 = 8\,\mathrm{pF}$ both in the simulations and in the experiments. By detailed comparisons between Figs. 7a and b, there is a difference in the number of the reflection maxima below the cut-off frequency. As we saw in the simulation of the variable pitch coils, the configurations of terminal wires could affect the reflection sensitively. For imperfect real coils, one can expect that the reflection shows maxima at the condition other than $\beta = n\pi$. We cannot determine β from the reflection maxima as described in Section 4.1 and Fig. 3.

The more reliable way to measure β is to look the transmission of a coil connected to coaxial cables having the much higher characteristic impedance than that of the coil. If we ignore the loss through the coil, the four terminal constants are expressed by the phase delay β and the effective impedance Z_{eff}:

$$A = \cos\beta, \tag{55}$$

$$B = \mathrm{j}Z_{\mathrm{eff}}\sin\beta, \tag{56}$$

$$C = \mathrm{j}Z_{\mathrm{eff}}^{-1}\sin\beta. \tag{57}$$

Under the conditions $\beta = n\pi$ (n integer), the transfer matrix becomes a unit matrix, i.e., $A = 1$, $B = C = 0$, so that the transmission also becomes a unity. The phase delay β can be measured from the frequencies where the transmission shows the maxima. The minimum of the transmission should appear when $\beta = (1/2)(2n+1)\pi$. From the minimum value of transmission T_{min}, the effective impedance of the coil Z_{eff} can be determined by using

$$Z_{\mathrm{eff}}/Z_0 = (1/|T_{\mathrm{min}}|) \pm \sqrt{(1/|T_{\mathrm{min}}|)^2 - 1}, \tag{58}$$

where the plus (minus) sign is applied for $Z_{\mathrm{eff}} > Z_0$ ($Z_{\mathrm{eff}} < Z_0$).

Fig. 7c shows the experimental and simulated transmissions of the coils with the characteristic impedance $30.4\,\Omega$ ($C_0 = 24\,\mathrm{pF}$) and $14.2\,\Omega$ ($C_0 = 56\,\mathrm{pF}$), put between $50\,\Omega$ coaxial cables. The frequencies of the first and the second transmission maxima agreed well between the experiments and the simulations. These results showed the simulations could reproduce the reliable values of the phase constant β at least in the low-frequency range. In the high frequency region, the simulated transmissions deviated from the experimental ones. The deviation might be caused by the finite inductance of the ground loops, which was not taken into account in the simulation. The experimental cut-off frequency of the $14.2\,\Omega$ ($n_{\mathrm{c}} = 1.5$) coil was almost the half obtained by the simulation, while the $30.4\,\Omega$ ($n_{\mathrm{c}} = 3$) coil showed much better agreements between the experiment and the simulation. When $n_{\mathrm{c}} = 1.5$, the coil divided the ground planes and they were connected together by a 15 mm wide copper film. The inductance between the upper and the lower ground might not be negligible.

Next, we will compare the RF field homogeneity. Fig. 8a shows the maximum and the minimum values of the simulated RF field for some C_0 and n_{c} values. As described in Section 4.3 and Fig. 5c, the amplitude of the RF field oscillates along the coil axis, the y-direction. The maximum and the minimum values were obtained by varying y in the 70% region of the total coil length. We also calculated the magnitude of the RF field as a function of the carrier frequency at the coil center by using the approximate Eq. (49). A thick line shows the result. It almost agrees with the maximum curve for $C_0 = 4.49\,\mathrm{pF}$, which satisfies the impedance matching condition. The maximum curves show the resonance type enhancement near the cut-off frequency. The minimum curves decrease monotonically and becomes zero near the cut-off frequency. The difference between these pair of curves corresponds to the inhomogeneity along the coil axis. The homogeneity is the best for $C_0 = 8\,\mathrm{pF}$ around 100 MHz while it becomes the best for $C_0 = 6\,\mathrm{pF}$ around 400 MHz.

The homogeneity and the magnitude of the RF field are easily checked by nutation experiments, where the signal is observed as a function of the excitation pulse length. We performed the experiments at the RF power 100 W and calculated the nutation curves for a sample in the 80% region of the total coil length and within a diameter 1.6 mm, which is equivalent to the experimental condition. The results are shown in Figs. 8b and c for the carrier frequencies 400 MHz (^{1}H) and 106 MHz (^{23}Na), respectively. Fig. 8b shows that the experimental RF fields of ^{1}H were slightly more inhomogeneous than the simulated ones. The magnitudes of the RF field were about 60 kHz in the experiments and 35–41 kHz in the simulations, respectively. If we consider the accuracy of the RF power measurements by an oscilloscope at 400 MHz, the discrepancy may not be so significant. The available RF field strength of the probe was enough for ordinary ^{1}H solid-state NMR experiments.

Both the experimental and the simulated nutation curves of ^{23}Na were almost sinusoidal, which indicated the good RF field homogeneity of the coils at this frequency. However, the RF field strength was about 11 kHz and slightly weak for solid ^{23}Na NMR samples. The typical RF field strength of commercial 5 mmϕ double or triple resonance MAS probe is 70 kHz/100 W for ^{1}H (400 MHz), and 35 kHz/100 W for ^{13}C (100 MHz). They have a twice better RF efficiency than the above transmission line NMR probe.

However, we can improve the RF efficiency either by decreasing the pitch of the coil or by decreasing the impedance of the coil, since the maximum RF field at

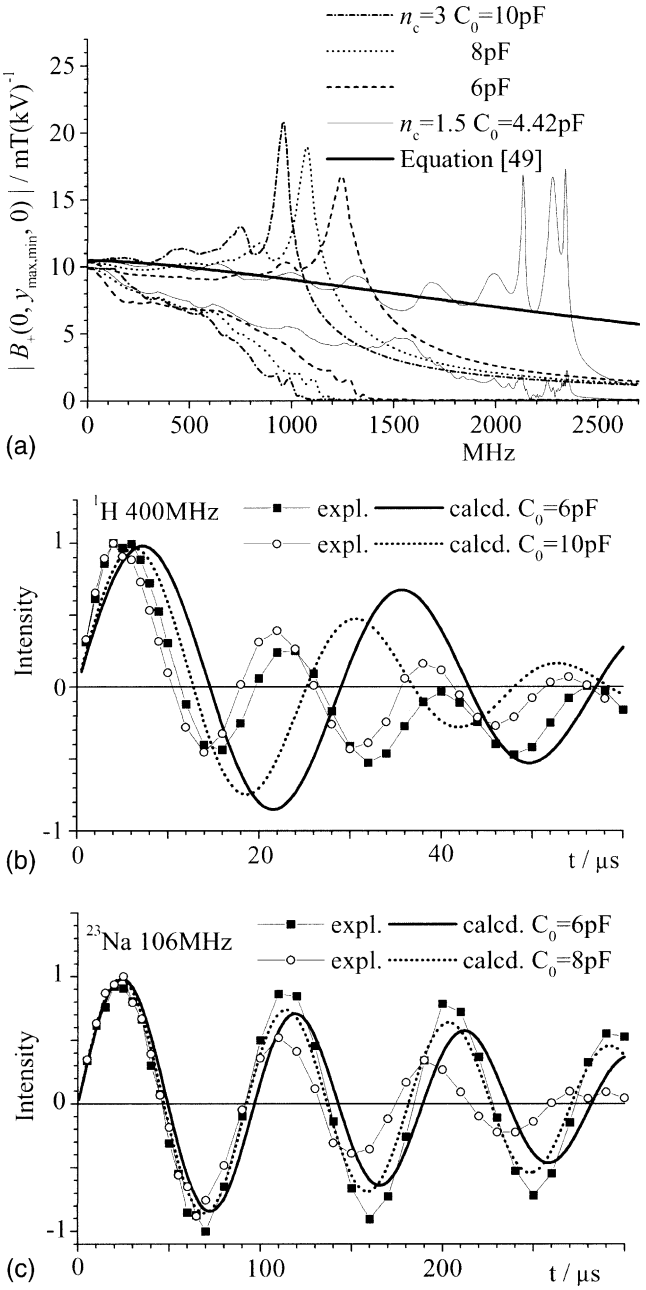

Fig. 8. The calculated RF field distributions in cylindrical transmission line coils and the comparisons between the calculated and the experimental nutation curves. The dimensions of the coils are the same as those given in Fig. 7. In (a), the maximum and the minimum values of the RF fields were calculated along the cylinder axis within a region ±35% of the coil length from the center. The RF field was also calculated by Eq. (49). In (b) and (c), the experimental and the calculated nutation curves are compared at the two resonant frequencies. The calculation assumed that the sample was placed in a diameter 1.6 mm and within 80% of the total coil length.

the zero carrier frequency is given by $|B_+|_{\max,\nu=0} = (\mu_0/p)\sqrt{(P_{\text{in}}/2Z_0)}$, where P_{in} is the input power. The signal-to-noise ratio (SNR) can be also improved by these methods, because it is proportional to the RF field strength divided by the input voltage. If we decrease the pitch, we must also decrease the radius of the coil to maintain the same inductance value. We did not try the first method, because it seemed to need more elaborate works to fabricate such a small coil, although it may not be impossible. Since the sample volume also becomes very small, the first method may be employed when a small amount of a sample is available. In the next section, we will consider the second method.

4.7. Impedance transformation by $\lambda/4$ cables

If we use a low-impedance coil to enhance the RF magnetic field strength, the cable impedance usually 50 Ω has to be transformed to the characteristic impedance of the coil, for example 12.5 Ω. The easiest method is inserting 25 Ω $\lambda/4$ cables between the coil and the ordinary 50 Ω cables (see Fig. 1c), although this method limits the usable carrier frequency to finite frequency bands around $(2n-1)\lambda/4$ frequencies. We simulated the performance of the 12.5 Ω probe including the $\lambda/4$ cable impedance transformers at the both ports. If the cables with a length l_T, a characteristic impedance Z_T, and the propagation constant γ_T are employed, the four terminal constants $A = D, B$, and C are transformed according to the following equations:

$$A' = A\cosh 2\gamma_T l_T + \frac{1}{2}\left(BZ_T^{-1} + CZ_T\right)\sinh 2\gamma_T l_T, \tag{59}$$

$$B' = AZ_T \sinh 2\gamma_T l_T + \frac{1}{2}\left(BZ_T^{-1} + CZ_T\right)Z_T \times \cosh 2\gamma_T l_T + \frac{1}{2}\left(BZ_T^{-1} - CZ_T\right)Z_T, \tag{60}$$

$$C' = AZ_T^{-1} \sinh 2\gamma_T l_T + \frac{1}{2}\left(BZ_T^{-1} + CZ_T\right)Z_T^{-1} \times \cosh 2\gamma_T l_T - \frac{1}{2}\left(BZ_T^{-1} - CZ_T\right)Z_T^{-1}. \tag{61}$$

At the frequencies where $\gamma_T l_T = (2n-1)\pi j/2$, $n = 1, 2, \ldots$, the characteristic impedance of the whole system is given by $Z' = \sqrt{B'/C'} = Z_T^2\sqrt{C/B} = Z_T^2/Z_{\text{eff}}$.

We have calculated the electrical characters of the whole probe circuit including the impedance transformers and a 50 Ω terminator, by combining Eqs. (59)–(61) and the method described in Section 2. We constructed the 12.5 Ω impedance probes using 25 Ω coaxial cables as impedance transformers. In Fig. 9a, we compare the simulated and the experimental reflections and the transmissions, when the length of the transformer cables was 0.55 m. The impedance matching frequencies were 94 and 280 MHz for the $\lambda/4$ and the $3\lambda/4$ conditions, respectively. The same coil was employed as the one with $C_0 = 56$ pF and $n_c = 1.5$ investigated in Fig. 7c. The simulated and the experimental curves agree well around the $\lambda/4$ frequency. However, the experimental curves show a shallower $|R|$ minimum

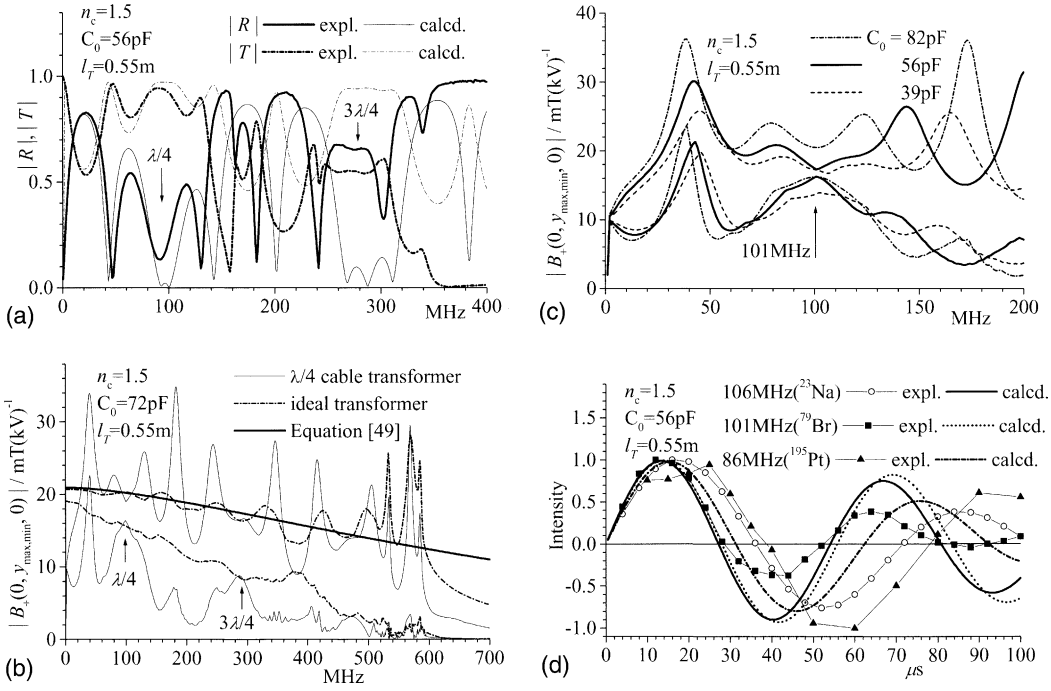

Fig. 9. The electrical characteristics and the field distributions in the low-impedance transmission line coils, which are transformed to 50 Ω by 25 Ω $\lambda/4$ cables. The length of $\lambda/4$ cables is $l_T = 0.55$ mm, which corresponds to a matching frequency 94 MHz. The dimensions of the cylindrical coils are the same as those described in Fig. 7. In (a), both the transmission and the reflection obtained from the measurements are compared with the results of the calculations. The maximum and the minimum RF fields were calculated for the same region as that defined in Fig. 8. Figure (b) compares the fields in a 12.5 Ω coil connected to $\lambda/4$ cable transformers (thin lines) to those in the coil connected to ideal 12.5 Ω ↔ 50 Ω transformers (dash-one-dot lines). The thick line was calculated by Eq. (49). In (c), the capacitor C_0 is varied to obtain the optimum homogeneity of the RF field. In (d), the nutation curves were measured at three carrier frequencies around the passband and are compared with the calculated results.

and a smaller $|T|$ maximum than those of the simulated curves around the $3\lambda/4$ frequency, although there are similarities between them. The reason of the disagreements may be the same as that of the discrepancy in Fig. 7c. Around the $3\lambda/4$ frequency, the effects of the incomplete fabrications like extra wire length at connections or nonideal ground become significant.

Besides these maxima, there are sharp transmission maxima or reflection minima at rather regular frequency intervals. For example, the simulated curve of $|R|$ shows minima at 43, 142, and 202 MHz. These frequencies are close to the peak frequencies, 56, 128, and 206 MHz in Fig. 7c, where the conditions $\beta = n\pi$ are satisfied. Since the probe circuit has much lower characteristic impedance than 50 Ω, it works as a resonator under the resonance conditions $\beta = n\pi$. This is the same phenomenon, which is applied to microstrip resonators in microwave circuits and optical mirror resonators.

The maximum and the minimum RF fields along the coil axis were calculated for the capacitance value $C_0 = 72$ pF which was obtained from the impedance matching condition $Z_{\text{eff}}(0) = 12.5\,\Omega$. The results are shown in Fig. 9b by thin lines. We also calculated the fields for a 12.5 Ω coil connected to ideal 50 Ω ↔ 12.5 Ω transformers. The ideal transformer can convert the input voltage and current of a 50 Ω port to a half and a twice at the 12.5 Ω output port, respectively. The RF field values per unit input voltage were obtained by multiplying 1/2 to the values calculated for a 12.5 Ω coil connected to a 12.5 Ω system, 12.5 Ω feeding/receiving cables, and a terminator. They are shown by dash-one-dot lines in Fig. 9b. The values obtained from Eq. (49) are also shown by a thick line.

At the impedance matching frequencies; 100 and 290 MHz for the $\lambda/4$ and $3\lambda/4$ conditions, respectively, the thin lines and the dash-one-dot lines coincide with each other. Eq. (49) predicted the maximum field values at these frequencies. The difference between the thin lines corresponds to the field inhomogeneity along the coil axis. It takes minima at the impedance matching frequencies and takes maxima at the resonance frequencies. The latter can be easily understood from the fact that the standing wave is dominant under the resonance conditions. The maximum field strength corresponds to the amplitude of the standing wave and the minimum field strength is given by the field value at the nodes. The values at the nodes are not zero, since $|B_+|$ contains the magnitudes of two RF field components along the x- and y-axes. Although the RF field becomes large at the resonance conditions, they are not suitable to NMR experiments because of the large field inhomogeneity.

Fig. 9c shows how the capacitor value affects the homogeneity of the RF field. The best homogeneity was obtained for $C_0 = 56\,\mathrm{pF}$, which is slightly lower than the value 72 pF for the impedance matching. The passband of this probe was estimated to be $101 \pm 10\,\mathrm{MHz}$. In this frequency region, the RF field distribution was within 30% of the average RF strength. The center of the band is slightly higher than the $\lambda/4$ frequency, 94 MHz for the cable length of 0.55 m. When the $\lambda/4$ cable length was increased, the bandcenter frequency decreased, while the optimum capacitor value $C_0 = 56\,\mathrm{pF}$ was not affected. To confirm the above simulation, we performed nutation experiments and compared the results with those by the simulations in Fig. 9d. The RF field of ^{79}Br at 101 MHz was 20 kHz/100 W in the experiment and agreed with the simulation. The field homogeneity was slightly worse in the experiment than that of the simulation. At the frequencies 86 and 106 MHz, the experimental RF field strengths were 13 and 15 kHz, respectively, which were 70% of the simulated values. When the $\lambda/4$ cable length was changed to 0.60 m, then the RF field strength of ^{195}Pt was increased to 20 kHz. Our simulations can predict the experimental performance of the probes with good accuracy.

5. Conclusion

In this publication, we made extensive simulations of the transmission line coils and compared the results with those obtained from analytical approximate equations. Electrical characteristics can be predicted from analytical expressions for a N-cascaded LC low-pass filter, where the inductance of each section is replaced by that of whole coil divided by N. There are three important parameters characterizing the transmission line coil; the effective impedance at zero frequency, $Z_{\mathrm{eff}}(0)$, the cut-off frequency, ν_{c}, and the phase constant, β, which are given by Eqs. (32)–(34).

The magnitudes of RF magnetic fields are well described by Eqs. (40), (41) and (49), (50) for flat and cylindrical transmission line coils, respectively. Since there is a phase delay $\beta/N \approx \nu/\nu_{\mathrm{c}}$ between currents flowing in neighboring coil sections, where ν is a carrier frequency, the magnitude of RF field in the coil decreases as a carrier frequency increases. The decay frequency ν_{d} is given by Eqs. (41) and (50), for flat and cylindrical transmission line coils, respectively. The diameter of the coil has to be very small to keep ν_{d} and ν_{c} much larger than a carrier frequency. The pitch and the effective impedance determine the RF field strength at a zero frequency. The RF field strength and the sensitivity of the probe were improved by using a low-impedance transmission coil and $\lambda/4$ cable impedance transformers. They were not necessary for ^{1}H experiments, but necessary for ^{195}Pt, ^{79}Br, and ^{23}Na experiments.

The RF field homogeneity in the transmission line coils was investigated by numerical calculations. The inhomogeneity of a cylindrical coil was similar to that of a flat coil. One important factor affecting the homogeneity is an impedance mismatch at the both ends of the transmission line coils. It causes reflections and a standing wave in the coil circuit, so that the magnitude of RF field oscillates along the coil axis. At low-carrier frequencies, the homogeneity can be improved by varying the pitch of the coil near the ends and reducing the standing wave. Another simple method is constructing a probe from a single π-section, since the current should be uniform over a single coil. However, the size of the coil has to be very small, since the inductance per section is limited by the impedance matching condition.

Although the transmission line probe accepts only a small sample volume as described above, it may allow several new wideband experiments on quadrupolar samples, metallic samples, ferromagnetic samples, or samples under a very large static magnetic field gradient. In quadrupolar samples containing half-integer nuclear spins, multifrequency irradiation [15,16], adiabatic frequency sweep [17–21], or fast amplitude modulation [22,23] have been employed for enhancements and assignments central transitions or excitations of multiple-quantum transitions. The larger bandwidth of the transmission line probe may enable experiments on quadrupolar nuclei with the larger quadrupolar couplings than those which have been studied by a resonant type probe. By a conventional resonant type probe, most of RF power might be reflected before reaching to a sample coil, when RF is modulated with the frequency larger than a probe bandwidth, i.e., a few hundred hertz. In metallic or magnetic samples, magnetic properties of the samples can depend on the strength of static magnetic field. In conducting samples, chemical shift depends on the field strength due to the de Haas van Alphen Effect (more generally Aharonov–Bohm effect) [24]. In ferrimagnetic metal clusters, the crossover between different magnetic levels takes place when static magnetic field is increased [25]. In such samples, there is an advantage in observing broadband spectra by a frequency-sweep method, since strength of a static magnetic field can be varied as an independent parameter. Another advantage is the possible use of the probe in correlation NMR experiments like high resolution two-dimensional NMR experiments [1]. Although it is not popular, the J-coupling might be important in conducting and magnetic fine particles [26].

There are still some rooms for a further implementation. Noise of NMR signals is determined by resistive components in a probe circuit. The two ports of a transmission line probe are terminated by a load and a transmitter (or a receiver). Receiving mode or transmitting mode are selected by RF switches (in our experiments by crossdiodes). The noise might be mainly generated by the load. If the load is cooled or the resistance of the load is

reduced by appropriate impedance transformations the noise might be reduced. In the transmission line probe, the load can be moved far from the sample coil and can be kept at a constant temperature by using a large heat bath. It may solve big temperature dependences of resistor materials at low temperature, although the appropriate material for load must be selected depending on the bath temperature. An ideal load must generate no thermal noise and absorb RF signals completely. Empolying superconductive circuits in the transmission line probes also may reduce noise of the whole the circuit. One big problem of superconducting NMR probes (mainly used for MRI) is that the probe Q becomes too high [27]. The bandwidth of the probe is typically about 40 kHz, which allows only the observation of solution-state ^{1}H signals. The transmission line probe has a fast recovery time like a coaxial cable as long as the impedance is properly matched with those of feeding and receiving cables. Thus superconducting transmission line probes might not have the high Q problem.

Physics of transmission lines also seems important to construct high frequency NMR probes. During the revision of the manuscript, we found an article, which investigates the wavelength compression of solenoidal coils at very high frequency over 1 GHz [28]. At this frequency, even normal solenoidal coils behave as transmission lines. Some parts of the calculations were similar to the present paper, although the intention was different from our paper.

Acknowledgments

This work is supported by Institute for Molecular Science, and was performed at the molecular cluster group in 2000–2001. We acknowledge Dr. Daisuke Kuwahara for lending us a network analyzer and a generous assistance for experiments. We also acknowledge Mr. G. Takamatsu (IMS), and Mr. M. Nagata, for helping us constructing the probes and preparing glass sample tubes, respectively. Some of chip capacitors were offered from Murata Electronics (www. murata.co.jp).

References

[1] R.R. Ernst, G. Bodenhausen, A. Wokaun, Principles of Nuclear Magnetic Resonance in One and Two Dimensions, Clarendon, Oxford, 1987.
[2] J.R. Pierce, Travelling-Wave Tubes, Van Nostrand, Princeton, NJ, 1950.
[3] R.H. Webb, Use of travelling wave helices in ESR and double resonance spectrometers, Rev. Sci. Instrum. 32 (1962) 732–737.
[4] F. Volino, F. Csakvary, P. Servoz-Gavin, Resonant helices and their application to magnetic resonance, Rev. Sci. Instrum. 39 (1968) 1660–1665.
[5] I.J. Lowe, M. Engelsberg, A fast recovery pulsed nuclear magnetic resonance sample probe using a delay line, Rev. Sci. Instrum. 45 (1974) 631–639.
[6] H.T. Stokes, T.A. Case, D.C. Ailion, NMR observations of molecular motions and Zeeman-quadrupole cross relaxation in 1,2-difluorotetrachloroethane, J. Chem. Phys. 70 (1979) 3563–3571.
[7] I.J. Lowe, D.W. Whitson, Homogeneous rf field delay line probe for pulsed nuclear magnetic resonance, Rev. Sci. Instrum. 48 (1977) 268–274.
[8] M.S. Conradi, Low-temperature NMR techniques, Concepts Magn. Reson. 5 (1993) 243–262.
[9] J. Haase, N.J. Curro, C.P. Slichter, Double ressonance probes for close frequencies, J. Magn. Reson. 135 (1998) 273–279.
[10] F.W. Grover, Inductance Calculations: Working Formulas and Tables, Dover, New York, 1962.
[11] J. Jin, Electromagnetic Analysis and Design in Magnetic Resonance Imaging, CRC Press, Boca Raton, 1999 (Chapter 4).
[12] M.N.O. Sadiku, Numerical Techniques in Electromagnetics, CRC Press, Boca Raton, 2001 (Chapter 5).
[13] S. Ramo, J.R. Whinnery, T. Van Duzer, Fields and Waves in Communication Electronics, Wiley, New York, 1993 (Chapter 4).
[14] S. Ramo, J.R. Whinnery, T. Van Duzer, Fields and Waves in Communication Electronics, Wiley, New York, 1993, pp. 476–478 (Chapter 9.8).
[15] H. Hatanaka, T. Terao, T. Hashi, J. Phys. Soc. Jpn. 39 (1975) 835.
[16] H. Hatanaka, T. Hashi, J. Phys. Soc. Jpn. 39 (1975) 1139.
[17] A.P.M. Kentgens, Quantitative excitation of half-integer quadrupolar nuclei by a frequency-stepped adiabatic half-passage, J. Magn. Reson. 95 (1991) 619–625.
[18] J. Haase, M.S. Conradi, C.P. Grey, A.J. Vega, Population transfers for NMR of quadrupolar spins in solids, J. Magn. Reson. A 109 (1994) 90–97.
[19] J. Haase, M.S. Conradi, E. Oldfield, Single- and double-resonance experiments of quadrupolar nuclei in solids using sensitivity enhancement of the central transition, J. Magn. Reson. A 109 (1994) 210–215.
[20] D. Iuga, H. Schaefer, R. Verhagen, A.P.M. Kentgens, Population and coherence transfer induced by double frequency sweeps in half-integer quadrupolar spin systems, J. Magn. Reson. 147 (2000) 192–209.
[21] H. Schaefer, D. Iuga, R. Verhagen, A.P.M. Kentgens, Population and coherence transfer in half-integer quadrupolar spin systems induced by simultaneous rapid passages of the satellite transitions: a static and spinning single crystal nuclear magnetic resonance study, J. Chem. Phys. 114 (2001) 3073–3091.
[22] S. Vega, Y. Naor, Triple quantum NMR on spin systems with $I = 3/2$ in solids, J. Chem. Phys. 75 (1981) 75–86.
[23] P.K. Madhu, A. Goldbourt, L. Frydman, S. Vega, Fast radio-frequency amplitude modulation in multiple-quantum magic-angle-spinning nuclear magnetic resonance: theory and experiments, J. Chem. Phys. 112 (2000) 2377–2391.
[24] R.G. Goodrich, S.A. Khan, J.M. Reynolds, Knight shift in cadmium: field and temperature dependences, Phys. Rev. B 3 (1971) 2379–2384.
[25] D. Gatteschi, R. Sessoli, Magnetic properties of large clusters, in: J.S. Miller, M. Drillon (Eds.), Magnetism: Molecules to Materials III, Wiley-VCH, Weinheim, 2002.
[26] C.P. Slichter, R. Corey, N. Curro, J. Haase, C. Milling, D. Morr, J.S.R. Schmalian, J-coupling in high temperature superconductors, Mol. Phys. 95 (1998) 897–906.
[27] S.M. Anlage, High temperature superconducting radio frequency coils for NMR spectroscopy and magnetic resonance imaging, in: H. Weinstock, M. Nisenoff (Eds.), Microwave Superconductivity, Kluwer Academic, Dordrecht, 2001.
[28] F. Engelke, Electromagnetic wave compression and radio frequency homogeneity in NMR solenoidal coils: computational approach, Concepts Magn. Reson. 15 (2002) 129–155.